PCCP

ROYAL SOCIETY OF CHEMISTRY

PAPER

View Article Online
View Journal | View Issue

Cite this: *Phys. Chem. Chem. Phys.*, 2024, **26**, 13790

Improving the estimation accuracy of confined vapor–liquid equilibria by fine-tuning the pure component parameter in the PC-SAFT equation of state

Aliakbar Roosta,[a] Sohrab Zendehboudi[b] and Nima Rezaei *[a]

Received 8th December 2023,
Accepted 3rd April 2024

DOI: 10.1039/d3cp05979k

rsc.li/pccp

We propose a thermodynamic model that combines the Young–Laplace equation and perturbed chain-statistical associating fluid theory (PC-SAFT) equation of state to estimate capillary condensation pressure in microporous and mesoporous sorbents. We adjust the PC-SAFT dispersion-energy parameter when the pore size becomes comparable to the molecular dimension. This modelling framework is applied to diverse systems containing associating and non-associating gases, various sorbents, and a wide range of temperatures. Our simulation results show that under extreme confinement, a higher value of the dispersion-energy parameter (ε) is required. Furthermore, using the experimental saturation pressure data for 18 different associating and non-associating confined fluids, we find that the shift in the PC-SAFT dispersion energy correlates with the ratio of the sorbent mean pore size to the PC-SAFT segment size (r_p/σ). By fitting to the capillary condensation data, the relative deviation between the confined and bulk PC-SAFT dispersion energy parameter is only 0.1% at $r_p/\sigma = 15$; however, this deviation starts to increase exponentially as r_p/σ decreases. For a sorbent with large pores, when $r_p/\sigma > 15$, the capillary condensation pressure results from our model are similar to the predictions from the Kelvin equation. Using a dataset containing 235 saturation pressure data points composed of 18 pure gases and 4 binary mixtures, the overall AARD% from our model is 12.26%, which verifies the good accuracy of our model. Because the mean sorbent pore radius (r_p), the PC-SAFT energy parameter (ε), and segment size (σ) are known *a priori*, our model estimates the corrected energy parameter for small pores and, thus, extends its applicability.

1 Introduction

Mesoporous and microporous adsorbents have extensive applications, including CO_2 capture,[1–3] drug delivery,[4,5] industrial wastewater treatment,[6–8] hydrogen production,[9,10] gas dehumidification,[11,12] energy storage,[13] reactions,[14] and catalysts.[15,16] Over the past two decades, considerable advancement has been made in understanding adsorption phenomena and the behavior of confined fluids in porous materials.[17] The adsorption process becomes complicated in microporous materials because of deviation in phase equilibria, including capillary condensation, upon extreme confinement (for pore radii of at least 0.5 nm). The Kelvin equation describes the curvature-dependency of vapor pressure for the nano-confined fluids;[18] it predicts that the vapor pressure of a confined wetting fluid becomes smaller than that of the bulk phase,[19] allowing capillary condensation in small pores. The Kelvin effect was directly measured for the first time by Fisher and Israelachvili.[20]

Despite the success of the Kelvin equation in estimating the vapor pressure of confined fluids, there is a debate on its validity for small pores with meniscus radii ranging 1–100 nm;[20] however, it has been experimentally verified that in principle, the thermodynamic basis for the Kelvin equation holds for the radii of curvature down to 4 nm.[21] The Kelvin equation is observed to overestimate capillary condensation pressure in microporous adsorbents; therefore, its thermodynamic framework must be modified under an extreme confinement (radii of curvature < 4 nm).[22] In recent years, various methodologies have emerged to improve the thermodynamic modeling performance for confined phase equilibria, including capillary condensation. In addition to including the capillary pressure effect in the phase equilibria framework, researchers have suggested several other modifications that consider, for example, the curvature-dependency of surface tension using the Tolman parameter,[23] heterogeneous density distribution due to solid–liquid interactions near the pore walls,[24] correction to the curvature value due to the adsorbed layer,[25] adjustments to the critical properties of the confined fluid,[26] and solid–confined liquid interaction energy.[27,28]

---

[a] Department of Separation Science, School of Engineering Science, LUT University, Lappeenranta, Finland. E-mail: aliakbar.roosta@lut.fi, nima.rezaei@lut.fi
[b] Department of Process Engineering, Memorial University, St. John's, NL, Canada

Most of the studies on confined phase equilibria are limited to the phase behavior application for reservoir fluids confined in tight shale formations.[29] In general, the confined phase equilibria are studied using thermodynamic frameworks such as density functional theory;[30–33] molecular dynamics simulation;[34,35] lattice Boltzmann method,[36] and equation of state (EoS) approach combined with Young–Laplace equation,[27,37,38] or modified Young–Laplace equation where the effect of the adsorbed layer is considered.[33,39] In this study, we use the EoS approach to model the capillary condensation pressure. In the literature, the Peng–Robinson equation of state (PR-EoS) is commonly used with the Young–Laplace equation, and the critical properties are adjusted under confinement.[40,41] Moreover, in some studies, the solid–liquid interaction energy is included in the van der Waals EoS thermodynamic modeling framework.[28,42] In general, the cubic EoSs are less accurate for modeling the behavior of associating fluids.[43] Also, they need critical properties as the input parameters; thus, the cubic EoS application can become challenging for the fluids for which the critical properties cannot be measured. For example, many ionic liquids start to decompose when the temperature approaches the normal boiling point.[44] To correct the cubic EoS models under extreme confinement, researchers often use the ratio of the Lennard-Jones size parameter to the pore radius ($\sigma_{\mathrm{LJ}}/r_{\mathrm{p}}$) to estimate the shift in the critical properties. Nonetheless, the Lennard-Jones potential is better suited for describing small nonpolar molecules.[45]

There are only a few studies in the literature on confined phase equilibria using thermodynamic EoS models that consider association. Xiong *et al.*[27] used cubic-plus association equation of state (CPA-EoS) to estimate confined phase equilibria for 10 non-associating fluids and two associating fluids (water and ethanol) in SBA-15, MCM-41, and Vycor® glass. They modified the energy parameter *a* in the CPA-EoS model by shifting the critical temperature and pressure upon confinement.[27] In another study, Tan and Piri[39] used perturbed chain statistical association fluid theory (PC-SAFT) EoS to model the phase behavior of different gases in SBA-15 and MCM-41. They also used a modified Young–Laplace equation by subtracting the thickness of the adsorbed layer prior to condensation from the pore radius value. Later, they used the PC-SAFT EoS to model the capillary condensation, including the retrograde condensation for reservoir fluids at the reservoir operating conditions.[46]

Unlike other EoS models, the PC-SAFT model does not rely on the critical properties and is suitable for both associating and non-associating molecules of varying sizes.[47,48] Therefore, we use the PC-SAFT model integrated with the Young–Laplace equation to calculate the capillary condensation pressure under confinement from dew point pressure calculations.[49] We test the thermodynamic model for various systems using associating and non-associating fluids at different temperature and composition levels. The pure and binary fluid mixtures that are studied are confined in micro- and mesoporous materials such as SBA-15, MCM-41, and Vycor® glass with a known pore size distribution, assuming a zero contact angle (complete wetting condition). For smaller pores, we adjust the PC-SAFT dispersion energy parameter (ε) to obtain more accurate capillary condensation pressure estimates from the model. Finally, we propose a general correlation for the adjustment factor ($\Delta\varepsilon$) with the ratio of the average pore radius to the PC-SAFT segment diameter (r_{p}/σ), which holds for all components tested. Because $\Delta\varepsilon$ can be obtained *a priori*, our predictive model can estimate the capillary condensation pressure for associating and non-associating fluids even when the pore size becomes comparable to the molecular size. The structure of our paper is as follows: after the introduction, Section 2 discusses the thermodynamic framework of the PC-SAFT model and capillary effects in the phase equilibria calculations; Section 3 presents the results for pure component and binary gas systems; finally, the conclusion remarks are given in Section 4.

2 Thermodynamic frameworks

2.1 Confined phase equilibria for multicomponent systems

The equality of fugacity for each mixture component in the available phases dictates the thermodynamics of phase equilibria. The equilibrium condition for the vapor–liquid equilibria (VLE) is given by eqn (1):[45]

$$f_i^{\mathrm{V}}\left(T^{\mathrm{V}}, P^{\mathrm{V}}, y\right) = f_i^{\mathrm{L}}\left(T^{\mathrm{L}}, P^{\mathrm{L}}, x\right) \tag{1}$$

where f_i is the fugacity of component i; T and P are the temperature and pressure, respectively; x and y represent the mole fractions in the liquid and vapor phases, respectively; and the superscripts V and L indicate the vapor and liquid phases, respectively. The fugacity of each component in the liquid and vapor phases can be written in terms of their fugacity coefficients using eqn (2):[45]

$$y_i\varphi_i^{\mathrm{V}}\left(T^{\mathrm{V}}, P^{\mathrm{V}}, y\right)P^{\mathrm{V}} = x_i\varphi_i^{\mathrm{L}}\left(T^{\mathrm{L}}, P^{\mathrm{L}}, x\right)P^{\mathrm{L}} \tag{2}$$

where φ_i is the fugacity coefficient of component i, that is computed using the PC-SAFT model.

The equilibrium conditions given by eqn (1) and (2) are valid for both the bulk and confined phase equilibria. In most applications, the thermal equilibrium condition predicts similar temperature values for the vapor and liquid phases ($T^{\mathrm{V}} = T^{\mathrm{L}}$), in both the bulk and confined systems. However, contrary to the bulk phase equilibria, the mechanical equilibrium condition in the confined fluids predicts different pressures for the vapor and liquid phases across a curved interface. The difference in the phase pressures is dictated by capillary pressure, which according to the Laplace equation, is related to the interfacial tension (γ) and the radius of curvature (r).[25] For a gas–liquid system confined in a cylindrical capillary tube and under equilibrium, the capillary pressure simplifies to the Young–Laplace equation, as presented in eqn (3):[50]

$$P^{\mathrm{V}} - P^{\mathrm{L}} = \frac{2\gamma}{r} = \frac{2\gamma\cos\theta}{r_{\mathrm{p}}} \tag{3}$$

γ is the interfacial tension; r_{p} is the capillary tube pore radius; and θ is the contact angle. Often, the calculations are simplified by assuming complete wetting in pores, which is quantified by zero contact angle.[27,39,51] We also make a similar assumption because the contact angle values are not available in the capillary condensation experiments conducted in nanocapillaries. Interfacial tension is an important parameter that affects the capillary pressure. In multicomponent systems, the solubility of a gas in the confined liquid changes the interfacial tension, and consequently, capillary pressure.[52] For a multicomponent system, the interfacial tension can be estimated using a so-called parachor method that is shown in eqn (4):[52]

$$\gamma = \left(\sum_i p_i\left[x_i\rho^{\mathrm{L}} - y_i\rho^{\mathrm{V}}\right]\right)^4 \tag{4}$$

where p_i represents the parachor of component i and ρ is the fluid density, which is estimated from the PC-SAFT model in this study.

The Kelvin equation is fundamental in interfacial thermodynamics, relating the saturation pressure of the confined and bulk fluids to curvature, as expressed in eqn (5):[50]

$$\ln\left(\frac{P}{P_\infty}\right)^{\mathrm{sat}} = -\frac{2\gamma v^{\mathrm{L}}}{RTr} \tag{5}$$

where γ represents the interfacial tension; v^{L} is the molar volume of the liquid phase; r is the mean radius of curvature for the condensed liquid; P^{sat} and P_∞^{sat} are the vapor pressure of confined and bulk phases, respectively; T represents the temperature; and R is the universal gas constant.

2.2 PC-SAFT model

We use PC-SAFT EoS to calculate the fugacity coefficient and density of confined fluids. The PC-SAFT model was proposed by Gross and Sadowski[47,48] in the context of molecular thermodynamics and statistical mechanics. It considers molecules as chains with a different number of segments and sizes interacting with each other. Because PC-SAFT considers the molecular interactions, it is especially suitable for calculating phase equilibria and physical properties of systems that involve associating fluids, polymers, and colloids.[47]

The PC-SAFT model is formulated using dimensionless residual Helmholtz energy contributions from hard-chain, dispersion, and association as illustrated in eqn (6):[47,48,53–55]

$$\tilde{a}^{\mathrm{res}} = \tilde{a}^{\mathrm{hc}} + \tilde{a}^{\mathrm{disp}} + \tilde{a}^{\mathrm{assoc}} \tag{6}$$

The dimensionless dispersion contribution term for the residual Helmholtz energy is given by eqn (7):[47]

$$\tilde{a}^{\mathrm{disp}} = -2\pi\hat{\rho}I_1\overline{m^2\varepsilon\sigma^3} - \pi\hat{\rho}\bar{m}C_1I_2\overline{m^2\varepsilon^2\sigma^3} \tag{7}$$

where $\hat{\rho}$ is the total number density of the molecules and is related to density and Avogadro's number (N_{A}) using eqn (8):

$$\rho\left(\frac{\mathrm{mol}}{\mathrm{cm}^3}\right) = \frac{\hat{\rho}\left(\mathrm{\mathring{A}}^{-3}\right)\times 10^{24}}{N_{\mathrm{A}}} \tag{8}$$

The intermediate variables in eqn (7) are defined by eqn (9)–(17):[47]

$$\begin{aligned} C_1 = \Bigg(&1 + \bar{m}\frac{8\xi_3 - 2\xi_3^2}{(1-\xi_3)^4} \\ &+(1-\bar{m})\frac{20\xi_3 - 27\xi_3^2 + 12\xi_3^3 - 2\xi_3^4}{((1-\xi_3)(2-\xi_3))^2}\Bigg)^{-1} \end{aligned} \tag{9}$$

$$\overline{m^2\varepsilon\sigma^3} = \sum_i\sum_j x_ix_jm_im_j\frac{\varepsilon_{ij}}{kT}\sigma_{ij}^3 \tag{10}$$

$$\overline{m^2\varepsilon^2\sigma^3} = \sum_i\sum_j x_ix_jm_im_j\left(\frac{\varepsilon_{ij}}{kT}\right)^2\sigma_{ij}^3 \tag{11}$$

$$\sigma_{ij} = \frac{\sigma_i + \sigma_j}{2} \tag{12}$$

$$\varepsilon_{ij} = \sqrt{\varepsilon_i\varepsilon_j}\left(1 - k_{ij}\right) \tag{13}$$

$$I_1 = \sum_{i=0}^{6} a_i\xi_3^{\,i} \tag{14}$$

$$I_2 = \sum_{i=0}^{6} b_i\xi_3^{\,i} \tag{15}$$

$$a_i = a_{0i} + \frac{\bar{m}-1}{\bar{m}}a_{1i} + \frac{\bar{m}-1}{\bar{m}}\frac{\bar{m}-2}{\bar{m}}a_{2i} \tag{16}$$

$$b_i = b_{0i} + \frac{\bar{m}-1}{\bar{m}}b_{1i} + \frac{\bar{m}-1}{\bar{m}}\frac{\bar{m}-2}{\bar{m}}b_{2i} \tag{17}$$

where m_i, σ_i and ε_i are the segment number per chain, segment diameter, and the dispersion-energy parameter for component i, respectively, and are among the PC-SAFT pure component parameters; and k is the Boltzmann constant. In addition, k_{ij} is the binary interaction parameter in the PC-SAFT model. The values of the model universal constants a_{0i}, a_{1i}, a_{2i}, b_{0i}, b_{1i}, and b_{2i} are available in the literature.[47]

Furthermore, ξ_n (n = 0, 1, 2, 3) and d_{i} are defined by eqn (18) and (19), respectively.

$$\xi_n = \frac{\pi\hat{\rho}}{6}\sum_i x_im_id_i^n \tag{18}$$

$$d_i = \sigma_i\left(1 - 0.12\mathrm{e}^{\frac{-3\varepsilon_i}{kT}}\right) \tag{19}$$

The dimensionless hard-chain and association contribution terms to the residual Helmholtz energy ($\tilde{a}^{\mathrm{hc}}$ and $\tilde{a}^{\mathrm{assoc}}$) are given in Appendix A.

To obtain the fugacity coefficient of a pure component or that of a component in the mixture, the following equations are employed:[47]

$$\ln\varphi_i = \frac{\mu_i}{kT} - \ln Z \tag{20}$$

$$\ln Z = 1 + \eta\left(\frac{\partial\tilde{a}^{\mathrm{res}}}{\partial\eta}\right)_{T,x} \tag{21}$$

$$\begin{aligned} \mu_i &= \tilde{a}^{\mathrm{res}} + (Z-1) + \left(\frac{\partial\tilde{a}^{\mathrm{res}}}{\partial x_i}\right)_{T,V,x_{k\neq i}} \\ &\quad - \sum_{j=1}^{N} x_j\left(\frac{\partial\tilde{a}^{\mathrm{res}}}{\partial x_j}\right)_{T,V,x_{k\neq j}} \end{aligned} \tag{22}$$

In eqn (20), Z and μ represent the compressibility factor and chemical potential, respectively. In addition, η is the packing fraction and is equal to ξ_3 (see eqn (18)). Details on the partial derivative terms in eqn (21) and (22) can be found in the literature.[47]

2.3 Dispersion-energy parameter of the PC-SAFT model for confined fluids

It is noted in the literature that including the capillary pressure in the framework of flash calculation alone does not always provide an accurate estimation of the confined vapor–liquid equilibria (VLE).[52] For pores of nm size, further adjustments to the confined VLE calculations using EoS models are required.[27,52] Yang *et al.*[52] used PR-EoS for confined phase equilibria and found it essential to adjust the critical pressure and critical temperature parameters, particularly when the ratio of pore radius to the Lennard-Jones diameter (r_p/σ_{LJ}) is less than 20. Furthermore, Xiong *et al.*[27] employed CPA-EoS for confined phase equilibria and concluded that for $r_p/\sigma_{LJ} < 10$, it becomes important to adjust the CPA energy parameter.

The molecular interactions between a confined fluid and the pore wall surface intensify the van der Waals forces of the fluid.[56,57] In a nanoconfined fluid, the effect of solid pore boundary is more pronounced, and the molecules experience attractive forces not only with each other but also with the molecules at the confining surfaces.[56,57] This allows molecules to come into a closer contact, enhancing the van der Waals interactions. The stronger van der Waals forces perturb the phase equilibrium by affecting the fugacity coefficient of the confined phase in eqn (2). In the PC-SAFT model, the van der Waals forces are incorporated in the dispersion energy term (eqn (7)). Hence, we adjust the dispersion energy parameter of the PC-SAFT model (ε) to obtain a better estimation of capillary condensation pressure in nanopores.

To model the system under extreme confinement, we use PC-SAFT confined dispersion energy parameter (ε_c) that is correlated to the conventional PC-SAFT dispersion-energy parameter (ε) through a so-called dimensionless adjustment factor ($\Delta\varepsilon$) as shown in eqn (23):

$$\varepsilon_c = \varepsilon(1 + \Delta\varepsilon) \tag{23}$$

The subscript c represents the confinement condition. Using experimental data of capillary condensation, we will later correlate the dimensionless adjustment factor ($\Delta\varepsilon$) to the ratio of pore radius to the PC-SAFT segment size (r_p/σ). To obtain the correction term, $\Delta\varepsilon$ for pure components under confinement conditions, experimental capillary condensation pressures are collected from literature for associating and non-associating pure and binary systems as detailed in Table 1. Then, the saturation pressure for the pure components is calculated from eqn (2) and (3) using the PC-SAFT EoS.

To find the adjustment factor ($\Delta\varepsilon$) for each component, genetic algorithm optimization method is used. We minimize

Table 1 List of experimental adsorption isotherms from which the capillary condensation data are derived

Adsorbate					
Name	Formula	Porous medium	Temperature (K)	Mean pore radius (nm)	Ref.
Nitrogen	N_2	MCM-48	55–115	1.9	58
Nitrogen	N_2	MCM-41	65–115	1.2–2.2	59 and 60
Nitrogen	N_2	SBA-15	68–120	3.0–3.9	59
Argon	Ar	MCM-41	57–135	1.2–2.2	41, 60 and 61
Argon	Ar	MCM-48	87	1.1–1.5	62
Oxygen	O_2	MCM-41	70–140	1.8, 2.2	60 and 61
Carbon dioxide	CO_2	MCM-41	200–260	1.8, 2.2	61 and 63
Carbon dioxide	CO_2	SBA-15	245–295	2.45, 3.3	64
Ethane	C_2H_6	SBA-15	263–300	3.04, 4.07	64
Ethylene	C_2H_4	MCM-41	144–148	1.8	60
Propane	C_3H_8	MCM-41	278.5–322.5	1.3–3.0	65
n-Butane	*n*-C_4H_{10}	MCM-41	281.8–301.4	1.3–3.0	65
n-Pentane	*n*-C_5H_{12}	MCM-41	258–298	1.4–3.2	63
n-Hexane	*n*-C_6H_{14}	MCM-41	298–323	1.2–2.2	66 and 67
n-Hexane	*n*-C_6H_{14}	SBA-15	293.2	3.4	68
c-Hexane	*c*-C_6H_{12}	SBA-15	293.2	3.4	68
3-Methyl pentane	C_6H_{14}	SBA-15	293.2	3.4	68
n-Heptane	*n*-C_7H_{16}	SBA-15	298.15–308.15	2.3–3.9	68 and 69
Benzene	C_6H_6	MCM-41	273.15–303.15	1.3–2.2	70 and 71
Toluene	C_7H_8	SBA-15	293.2	3.4	68
Methanol	CH_3OH	MCM-41	298	1.2–2.2	71
Ethanol	C_2H_5OH	MCM-41	273.15–303.15	1.3–2.1	70
Water	H_2O	MCM-41	298.2	1–2.1	72
Water	H_2O	SBA-15	293.2–298.2	2.5–3.3	72 and 73
Water	H_2O	OMC	294.5	3.1–4.6	74
Water	H_2O	MCM-48	293.15	1.4	73
Methane + Ethane	$CH_4 + C_2H_6$	SBA-15	236–277	3.28	75
Methane + Ethane	$CH_4 + C_2H_6$	MCM-41	264.75	1.95	76
Methane + Carbon dioxide	$CH_4 + CO_2$	SBA-15	240–280	3.28	75
Ethane + Carbon dioxide	$C_2H_6 + CO_2$	MCM-41	264.6	1.35	77
Nitrogen + Water	$N_2 + H_2O$	Mica	294	0.5–3.0	78

the average absolute relative deviation (AARD) between the experimental and computed capillary condensation pressure data as the objective function, as shown in eqn (24).

$$\mathrm{AARD} = \frac{1}{\mathrm{NP}}\sum_{n}\frac{\left|P_{\mathrm{ads}}^{\mathrm{exp}} - P_{\mathrm{ads}}^{\mathrm{cal}}\right|}{P_{\mathrm{ads}}^{\mathrm{exp}}} \qquad (24)$$

NP is the number of datapoints, and P_{ads} is the capillary condensation pressure. The superscripts exp and cal indicate experimental and calculated (from the model), respectively. To use the PC-SAFT EoS, the model parameters for all components are required, which are obtained from literature and summarized in Table 2.

To create a generalized correlation for $\Delta\varepsilon$, we relate the dimensionless adjustment factor to the ratio of r_p/σ; r_p represents the mean pore radius; and σ is the segment diameter in the PC-SAFT EoS. Therefore, for the situations when the pore radius becomes comparable to the molecular diameter, the inclusion of capillary pressure in the VLE calculations alone is not sufficient to predict the confined phase behavior. In such cases, we modify ε to improve the accuracy of the confined VLE calculation for the extremely small pores.

3 Results and discussion

3.1 Capillary condensation pressure for pure gases

The dimensionless energy adjustment factor ($\Delta\varepsilon$) is determined using a dataset comprising 78 data points, which include 18 different components such as permanent and noble gases, various hydrocarbons, alcohols, and water. This adjustment factor is calculated individually for all components to predict the capillary condensation pressure experiments at given pore sizes. We find $\Delta\varepsilon$ to be independent of temperature. The resulting adjustment factor ($\Delta\varepsilon$) is shown in Fig. 1 as a function of the dimensionless parameter r_p/σ. Fig. 1 shows positive values for the adjustment factor, indicating that the dispersion-energy parameter for the confined fluids is greater than that of the bulk fluids ($\varepsilon_c > \varepsilon$). In addition, Fig. 1 demonstrates that the adjustment factor increases exponentially as the r_p/σ ratio decreases. Conversely, the adjustment factor approaches zero with the increase in the r_p/σ ratio. It signifies that the PC-SAFT dispersion-energy parameter for the confined fluids approaches that of the bulk fluids when pores become large compared to the molecular dimension ($r_p/\sigma > 15$).

This adjustment factor, as shown in Fig. 1, fits well to (r_p/σ), which considers the ratio of characteristic sizes of porous media (r_p: pore radius) and the confined fluid molecular size (σ: the PC-SAFT segment diameter). Both r_p and σ are known *a priori* for most fluids, and the correlation in eqn (25) provides a general modification, which is valid for the wide ranges of temperature, pressure, and components used, as summarized in Table 1.

In addition, to provide a generalized representation of the adjustment factor, a correlation is introduced to link the (r_p/σ) ratio to the adjustment factor, as given by eqn (25).

$$\Delta\varepsilon = \frac{\varepsilon_c - \varepsilon}{\varepsilon} = 0.4386\mathrm{e}^{-0.4042\left(\frac{r_p}{\sigma}\right)} \qquad (25)$$

The *t*-test analysis on the regression parameters shows that the coefficient and exponent parameters are statistically significant at a 95% confidence level. According to the correlation, when the ratio (r_p/σ) = 15, the adjustment factor ($\Delta\varepsilon$) is only 0.001. This implies that the PC-SAFT dispersion-energy

Table 2 PC-SAFT pure component parameters and parachor

	PC-SAFT pure parameters							
Component	m	σ	ε/k (K)	k^{AB}	ε^{AB}/k (K)	Ref.	Parachor	Ref.
Non-associating fluids								
N_2	1.2053	3.3130	90.96	—	—	47	60.5	27
Ar	0.9285	3.4784	122.23	—	—	47	54.0	27
O_2	1.1335	3.1947	114.43	—	—	79	53.6	27
CO_2	2.0729	2.7852	169.21	—	—	47	77.5	80
CH_4	1.0000	3.7039	150.03	—	—	47	72.6	80
C_2H_6	1.6069	3.5206	191.42	—	—	47	110.5	80
C_2H4	1.5930	3.4450	176.47	—	—	47	99.5	80
C_3H_8	2.0020	3.6184	208.11	—	—	47	150.8	80
n-C_4H_{10}	2.3316	3.7086	222.88	—	—	47	190.3	80
n-C_5H_{12}	2.6896	3.7729	231.20	—	—	47	231.0	80
n-C_6H_{14}	3.0576	3.7983	236.77	—	—	47	270.8	80
c-C_6H_{12}	2.5303	3.8499	278.11	—	—	47	241.7	80
C_6H_{14}	2.8852	3.8605	240.48	—	—	47	267.9	80
n-C_7H_{16}	3.4831	3.8049	238.40	—	—	47	311.3	80
C_6H_6	2.4653	3.6478	287.35	—	—	47	205.7	80
C_7H_8	2.8149	3.7169	285.69	—	—	47	245.7	80
Associating fluids (2B scheme)								
CH_3OH	1.5255	3.2300	188.90	0.035176	2899.5	48	*	80
C_2H_5OH	2.3827	3.1771	198.24	0.032384	2653.4	48	**	80
H_2O	1.0656	3.0007	366.51	0.034868	2500.7	48	***	27

The parachor (p) for methanol, ethanol, and water are obtained from the literature and are correlated with temperature (T in K): * $p = 82.07 + 0.0212T$, ** $p = 113.6 + 0.0602T - 5.013 \times 10^{-5}T^2$, and *** $p = 91.7714 - 0.3517T + 1.176 \times 10^{-3}T^2 - 1.7636 \times 10^{-6}T^3 + 1.0023 \times 10^{-9}T^4$.

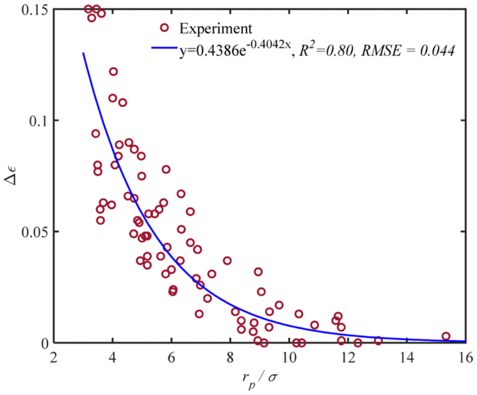

Fig. 1 Adjustment factor $\Delta\varepsilon$ of PC-SAFT for confined fluids *vs.* r_p/σ, a comparison between data and proposed correlation using 18 different adsorbate species, six different adsorbents, and at different ranges of temperature and pore size, as listed in Table 1.

parameter for the confined fluids is 99.9% of that for the bulk fluid ($\varepsilon_c = 0.999\varepsilon$). Therefore, for $(r_p/\sigma) > 15$, there is no need for adjusting the PC-SAFT dispersion energy parameter to estimate the capillary condensation pressure. Note that for the range of pore radius corresponding to $15 < (r_p/\sigma) < 100$, capillary pressure should still be integrated with the PC-SAFT model to accurately estimate the capillary condensation pressure; however, using the PC-SAFT dispersion energy parameter from bulk (ε) is satisfactory. For $(r_p/\sigma) < 15$, confined VLE phase equilibria predictions using the PC-SAFT model deviate from experimental data; we find that by using the confined dispersion energy parameter (ε_c) instead of the conventional dispersion energy parameter (ε) in the PC-SAFT model, the VLE prediction error reduces significantly.

In the following, we compare the experimental adsorption saturation pressure data for pure fluids with the proposed model. We use the PC-SAFT model with the Young–Laplace equation and assume complete wetting conditions. The proposed correlation shown in eqn (25) is used to modify the PC-SAFT EoS dispersion energy parameter when the pore size becomes comparable to the molecular dimension. Using the thermodynamic framework discussed and performing dew point calculations, we estimate the mean pressure at which capillary condensation occurs in different mesoporous silica and at different temperature levels.

Using the entire dataset listed in Table 1, the estimated capillary condensation pressure values from our thermodynamic model are compared with the experimental data for 18 different pure gases at various temperatures and sorbent pore sizes, as illustrated in Fig. 2a. Using 235 data points gathered in our dataset from the literature, the AARD% value of 12.26% is achieved. The maximum relative deviation is observed in the case of benzene (C_6H_6) in MCM-41 with a pore radius of 1.3 nm and at a temperature of 273.15 K. Although the AARD% value for the maximum deviation is relatively large, the absolute error value is low; in this system, the experimental capillary condensation pressure is only 0.47 kPa, while the model estimation is 0.21 kPa, resulting in the maximum RD% of 57%. To show the importance of using the adjustment factor, we compare the experimental adsorption saturation pressure data for pure fluids with the model by employing the conventional dispersion energy parameter (ε), as shown in Fig. 2b. Consequently, an AARD% value of 40.28% is attained. A comparison of the AARDs reveals a notable enhancement in the adsorption saturation pressure predictions for pure fluids with the current model. Another observation arising from the comparison between Fig. 2a and b is that using the conventional dispersion energy parameter (ε) results in an overestimation of the adsorption saturation pressure. This overestimation is evident in Fig. 2b, where most data points lie above the $y = x$ line.

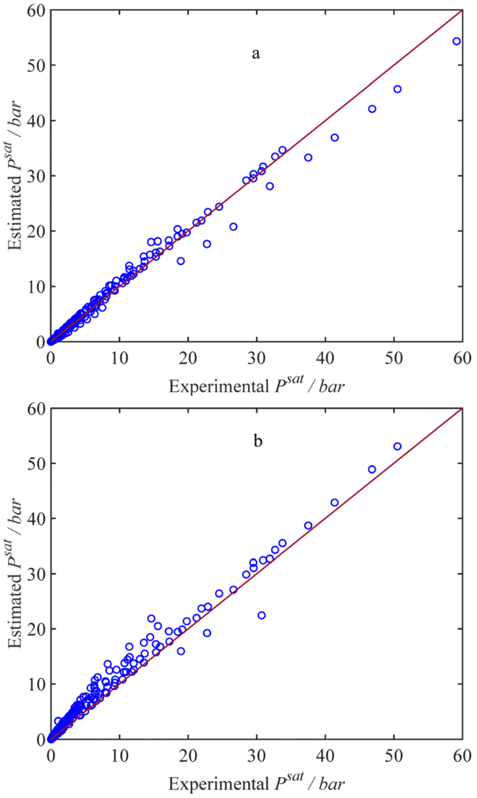

Fig. 2 Estimated and experimental confined saturation pressure for 235 datapoints that include 18 different pure gas components at various temperatures and porous materials, as listed in Table 1. Markers: datapoints, solid line: $y = x$, (a) with ε_c, (b) with ε.

To show the trends in capillary condensation pressure with temperature for different gases and for porous media with different average pore sizes, the model results are compared to the experimental data in Fig. 3. The solid lines show the saturation pressure of confined fluids from the model; the dashed lines represent the saturation pressure for the bulk condition; and the symbols denote the experimental data for capillary condensation pressure. Fig. 3 covers the adsorbate-adsorbent literature data for 13 different pure gas components, including associating fluids (such as water and alcohols) and non-associating fluids (such as the atmospheric gases and hydrocarbons). The capillary condensation pressure data from the literature are related to different porous materials such as MCM-41, MCM-48, OMC, Mica, and SBA-15 with different pore

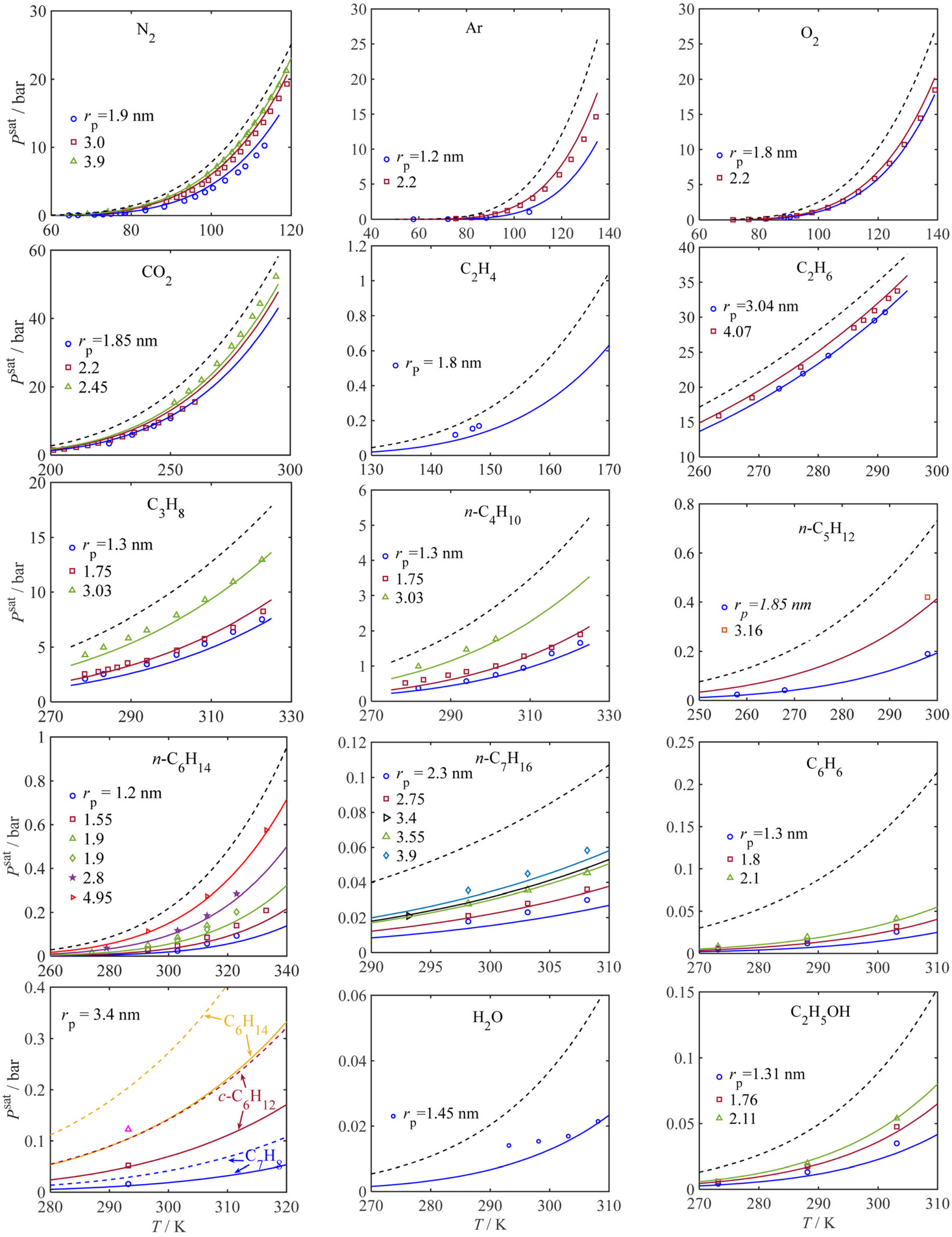

Fig. 3 Pure component condensation pressure for bulk and confined fluids from the current model and experimental data. Symbols: experiment, solid lines: model for confined fluid, and dashed line: bulk. Data sources: (N_2) ○,[58] □, Δ;[59] (Ar) ○,[60] □;[61] (O_2) ○,[60] □;[61] (CO_2) ○,[63] □,[61] Δ,[64] (C_2H_6),[64] (C_3H_8),[65] (n-C_4H_{10}),[65] (n-C_5H_{12}),[63] (n-C_6H_{14}) □ and ▷,[66] others,[67] (n-C_7H_{16}) ▷[68] others,[69] (C_2H_5OH),[70] (C_6H_6),[70] (H_2O),[73] (c-C_6H_{12}),[68] (C_6H_8),[68] (C_6H_{14}).[68]

sizes. Fig. 3 explores the influence of temperature and pore radius size on the capillary condensation pressure for various gas components, showing an excellent fit to the experimental data for all components tested. As expected, with an increase in temperature, the condensation pressure increases for a given pore size. Also, from Fig. 3, it follows that the rate of change (increase) in condensation pressure increases with temperature; at a given temperature, the rate of change in saturation pressure with temperature decreases under confinement such that as the pore size decreases, the rate of change in the capillary condensation pressure with temperature decreases. Also, in agreement with the Kelvin equation, at a given temperature, the saturation pressure is less for smaller pores. Alternatively, to achieve the same saturation pressure, a higher temperature is required when pores become smaller.

Furthermore, to assess the significance of our fine-tuned model, we compare capillary condensation pressure from the Kelvin equation (eqn (5)) and experiments with our model with and without adjustments to the dispersion energy parameter in Fig. 4 (by employing ε_c and ε, respectively). According to Fig. 4, the ratio of the confined saturation pressure to the bulk saturation pressure is plotted against the pore radius. The comparison is made for C_6H_6 and CH_3OH at 298 K,[71] and H_2O at 294.5 K.[74] Fig. 4 shows that the Kelvin equation and the current model without adjusting the dispersion energy parameter, both start to overestimate the saturation pressure when pores become small while our model (using ε_c) consistently provides a significantly better agreement with the experimental data even for smaller pore sizes. An analysis of the results in Fig. 4 shows that for C_6H_6, our model gives an AARD of 14.71%, while the Kelvin equation results in a notably higher AARD of 124.03%. In the case of CH_3OH, our model yields an AARD of 13.34%, whereas the Kelvin equation leads to a comparatively higher AARD of 48.20%. For H_2O, our model shows an exceptionally low AARD of 0.75%, while the Kelvin equation results in an AARD of 1.96%. In Fig. 4, we also show the location of $(r_p/\sigma) = 15$, at which the dispersion-energy parameter for the confined fluid is nearly identical to that of the bulk fluid ($\varepsilon_c = 0.999\varepsilon$). As observed in Fig. 4, for larger pores where $(r_p/\sigma) > 15$, the results from the Kelvin equation and our model are similar.

As discussed in Section 2.3, we adjust the dispersion energy parameter (ε) in the PC-SAFT model to address the increased van der Waals interactions upon fluid confinement. Fig. 5 represents the impact of adjusting the dispersion energy parameter on the van der Waals interactions for confined fluids. In this figure, we plot the ratio of the dispersion contribution to the Helmholtz energy for confined water to that of bulk fluid against the dimensionless variable (r_p/σ) with and without the correction for the dispersion energy parameter. The adjusted dispersion energy parameter is shown with ε_c in which the subscript c highlights correction for confinement condition, and the conventional dispersion energy parameter is shown with ε, which represents its value for the bulk phase.

When correcting for the confinement effects by using ε_c instead of ε, the model predicts an interplay between two conflicting factors that together affect $\tilde{a}^{\text{disp}}$ with varying the pore size. When decreasing the pore radius of a nanoconfined fluid, the adjusted PC-SAFT model uses a larger value for the dispersion energy parameter (ε_c), as proposed in Fig. 1, which increases $\tilde{a}^{\text{disp}}$ as it is expected from eqn (7). On the contrary, when decreasing the pore radius, the Young–Laplace equation predicts a lower pressure for the wetting liquid at a fixed gas pressure. At a lower liquid pressure, the number density decreases (in eqn (8), also reducing the intermediate terms I_1, I_2, and ξ_n in eqn (14) and (18), respectively), which reduces $\tilde{a}^{\text{disp}}$ accordingly. The overall observation is an increase in the dispersion contribution to the Helmholtz energy of the confined fluid, which is in agreement with the literature.[56,57] In the conventional modelling approach using ε (knowing that $\varepsilon < \varepsilon_c$), the PC-SAFT model overlooks the van der Waals interactions for the liquid molecules and pore surface that is expected for confined fluids. Thus, as can seen in Fig. 5, when using the conventional energy parameter ε in the PC-SAFT model, the $\tilde{a}^{\text{disp}}$ term for the nanoconfined fluid can become less than that of the bulk phase. The reason is that, in this case, the effect of confinement is only implemented through reduced liquid pressure (that eventually approaches a negative value) from the Young–Laplace equation, which consequently reduces $\tilde{a}^{\text{disp}}$.

3.2 Capillary condensation pressure for binary gas mixtures

As previously explained, the capillary condensation pressure of mixtures under confinement conditions can be determined by performing dew point calculations using an EoS in conjunction with the Young–Laplace equation. To assess the model's predictive capabilities in estimating the capillary condensation pressure in binary mixtures, we compare experimental capillary condensation pressure data with those from our model. However, compared to pure gases, the experimental data on capillary

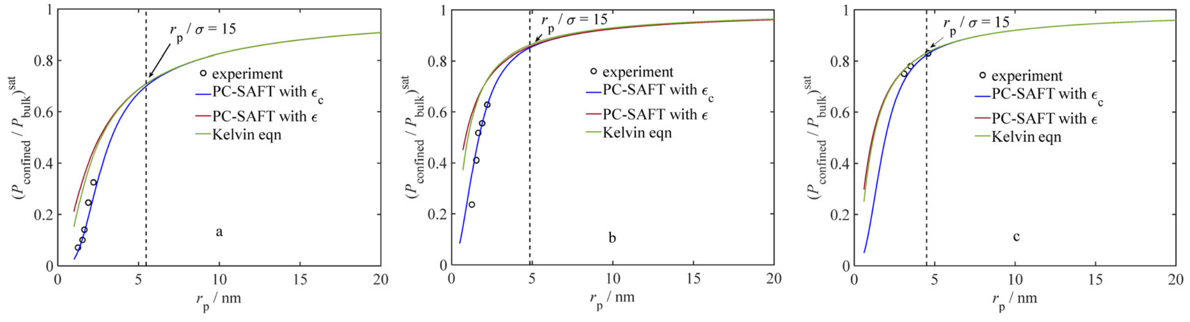

Fig. 4 Ratio of confined saturation pressure to bulk saturation pressure *vs.* pore radius; a comparison between the current model (with and without ε adjustment) and experiments: (a) C_6H_6 at 298 K,[71] (b) CH_3OH at 298 K,[71] (c) H_2O at 294.5 K.[74]

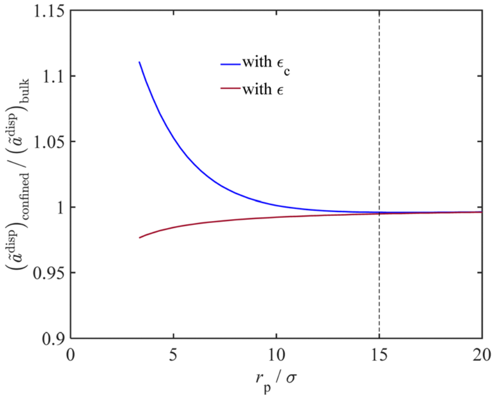

Fig. 5 The ratio of the dispersion energy of confined water to that of bulk water *vs.* the dimensionless variable r_p/σ, with and without ε adjustment.

condensation pressure of binary mixtures in porous materials are rather limited.

The binary interaction parameter of the PC-SAFT model (k_{ij}) for the confined fluid is adopted from those related to the bulk condition, as listed in Table 3. For mixtures of C_2H_6 + CO_2 and N_2 + H_2O, the binary interaction parameters are estimated due to the lack of available data in the literature. The comparisons between the current model results and experimental data are visualized in Fig. 6–9 for four different binary systems. Overall, excellent model predictions are observed when compared to the experimental data of the binary mixtures.

Fig. 6 shows a *P–T* diagram of capillary condensation pressure for binary gas mixtures at different temperatures; the corresponding dew pressure curves for these mixtures in the bulk phase (using PC-SAFT model) are also shown for comparison. The sorbent used in Fig. 6 is SBA-15 with an average pore radius of 3.28 nm, and the binary mixtures are CH_4 + C_2H_6 (15% CH_4) and CH_4 + CO_2 (12% CH_4). The binary interaction parameter is set to zero, which is consistent with the literature reports.

Fig. 6 reveals a remarkable agreement between the results obtained from our model and the experimental data. The results show that under confined conditions in SBA-15, the capillary pressure values for these binary mixtures are consistently lower by approximately 2.0 to 4.4 bar compared to bulk conditions at all temperature levels studied in this work. This agreement highlights the model's ability to predict the capillary condensation pressure in these mixtures effectively.

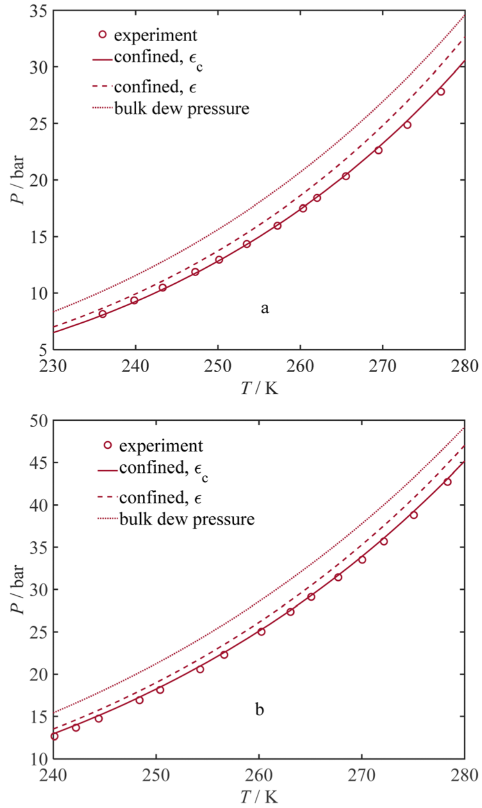

Fig. 6 Saturation pressure of isochoric binary gas mixtures *versus* temperature in bulk and in SBA-15: (a) CH_4 + C_2H_6 with x_{CH_4} = 0.15 and r_p = 3.28 nm, (b) CH_4 + CO_2 with x_{CH_4} = 0.12 and r_p = 3.28 nm; symbols: experimental data under confinement condition from ref. 75.

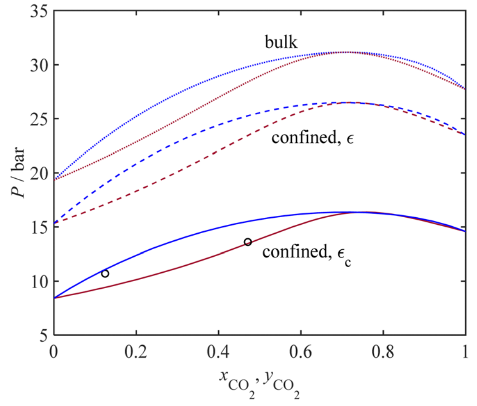

Fig. 7 *P-xy* diagram for C_2H_6 + CO_2 mixture at 264.6 K and r_p = 1.35 nm, under bulk and confined (with and without ε adjustment) conditions in MCM-41; symbols: experimental data under confinement condition from ref. 77.

Table 3 Binary interaction parameters of PC-SAFT at the bulk condition

Mixtures	k_{ij}	Ref.
CH_4 + C_2H_6	0	81
CH_4 + CO_2	0.065	47
C_2H_6 + CO_2	0.085	This work
N_2 + H_2O (2B scheme)	−0.055	This work

Fig. 7 presents a *P-xy* diagram for the C_2H_6 + CO_2 binary system at 264.6 K under bulk conditions (dashed lines) and under confinement conditions (solid lines). The sorbent is MCM-41, with an average pore radius of 1.35 nm. Fig. 7 displays a comparison between our model results obtained and the limited experimental data for adsorption capillary pressure. Despite the relatively narrow two-phase region band in Fig. 7, our results show a good agreement between the dew curve obtained by the model under confinement conditions (represented by the dark red solid line) and those limited

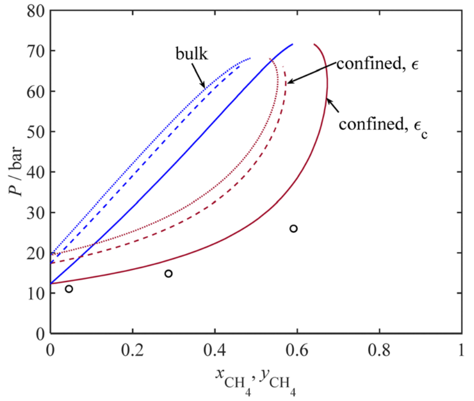

Fig. 8 P-xy diagram for the CH_4 + C_2H_6 mixture at 264.75 K and r_p = 1.95 nm under bulk and confined (with and without ε adjustment) conditions in MCM-41; symbols: experimental data under confinement condition from ref. 76.

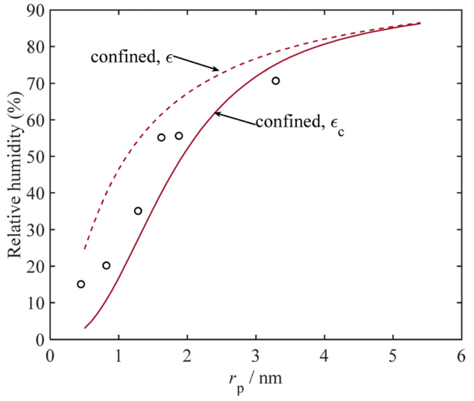

Fig. 9 Relative humidity required for H_2O condensation in a binary mixture of H_2O + N_2 in mica with different pore sizes at 294 K and the atmospheric pressure from model and experimental data.[78]

experimental data. Furthermore, a comparison between the confinement and bulk conditions highlights that the dew pressure under confinement is consistently lower by about 10 and 14 bar, respectively. This significant reduction in the dew pressures for the confined compared to the bulk phases is attributed to the small pore size (1.35 nm) of the MCM-41 adsorbent used.

Fig. 8 presents a comparison between the *P-xy* diagram for the bulk (dashed lines) and confined (solid lines) mixtures of CH_4 + C_2H_6 at 264.75 K and experimental adsorption capillary pressure data using MCM-41 with an average pore radius of 1.95 nm. According to Fig. 8, a good agreement is observed between the experimental results and the predicted dew data under confinement conditions, represented by the dark red solid line.

Furthermore, a comparison between the two-phase region under confinement conditions and bulk conditions reveals a notable shift of the *P-xy* diagram to higher temperature values. As it can be seen in Fig. 8, for mixtures with $x_{CH_4} > 0.55$, condensation does not occur at the bulk condition. However, for the confined mixtures with a CH_4 mole fraction of up to 0.67, condensation can still occur. For instance, at a temperature of 264.75 K, a mixture with a CH_4 mole fraction of 0.6 does not condense under the bulk conditions. However, the experiments show that it can be condensed at 26 bar; our model estimates the condensation pressure to be 37 bar in MCM-41 with an average pore size of 1.95 nm. This observation underscores the significant impact of confinement on the phase behavior of these mixtures.

Capillary condensation has applications in dehumidification and atmospheric water harvesting.[82] Fig. 9 illustrates the relative humidity level that is required for water condensation from a binary mixture of H_2O + N_2 at 294 K using mica as the adsorbent. As depicted in Fig. 9, the experimental data closely matches the results obtained from our thermodynamic model. These findings, as evident in Fig. 9, suggest that the wet nitrogen gas mixture can undergo dehumidification under ambient conditions in mica, even when the relative humidity percent for nitrogen is as low as 10%, which exists in arid climate conditions.

4 Conclusions

The importance of capillary condensation in micro- and mesoporous sorbents has motivated us to build a reliable model that can predict the capillary condensation pressure of associating and non-associating fluids. Our thermodynamic model uses PC-SAFT EoS and includes the effect of capillary pressure on dew point pressure by including the Young–Laplace equation for fluids confined in different sorbents such as MCM-41, MCM-48, SBA-15, mica, and Vycor® glass, and at different temperature values. A dataset of 235 capillary condensation data is collected for 18 pure gases (including permanent gases, hydrocarbons, alcohols, and water) and four binary gas mixtures (CH_4/C_2H_6, CH_4/CO_2, C_2H_6/CO_2, and N_2/H_2O), in sorbents with various mean pore sizes in the range 1 nm to 5 nm, under different temperature conditions.

To enhance the model accuracy, we adjust the PC-SAFT dispersion-energy parameter (ε) for confined fluids when the pore size becomes comparable to the adsorbate molecular size. By fitting the experimental data of capillary condensation pressure, our model results demonstrate that for the confined fluids, a higher PC-SAFT energy parameter should be used. Also, we find that the energy parameter increases as the sorbent pores become smaller. To extend the predictability of our model under extreme confinement, we develop a correlation that estimates the adjusted PC-SAFT energy parameter from *a priori* model and sorbent data. Using 78 experimental data for the 18 pure fluids, the adjustment factor (ε) of the PC-SAFT dispersion-energy parameter is found to correlate with the ratio of the sorbent mean pore radius to the PC-SAFT segment diameter (r_p/σ). This modification to the PC-SAFT energy parameter significantly improves the accuracy of calculations, especially for sorbents that feature small pores such that $(r_p/\sigma) < 15$.

The modification is however not required for larger pores. We conclude that for $(r_p/\sigma) \geq 15$, the capillary condensation pressure behavior from our model behaves similar to the Kelvin equation.

To assess the reliability of our model, we predict the dew point conditions for the bulk and confined fluids and compare them to the experimental data. The results show that the overall AARD% is 12.3% for a total of 235 data points, revealing an acceptable accuracy. We also compare our model results with those from the Kelvin equation. The values of AARD% in the ratio of confined-to-bulk saturation pressure for pure C_6H_6, CH_3OH, and H_2O are 14.71%, 13.34%, and 0.75%, respectively, using our model, and 124.03%, 48.2%, and 1.96%, respectively, using the Kelvin equation. Moreover, we employ our model to estimate the saturation pressure for four binary gas mixtures for which the PC-SAFT binary interaction parameters are taken from bulk conditions. The model results show that after correcting the PC-SAFT binary interaction parameter, the capillary condensation pressures obtained from the fine-tuned model match exceptionally well with the experimental data.

Author contributions

Aliakbr Roosta: conceptualization, data collection, programming, analysis, writing – review and editing. Sohrab Zendehboudi: analysis, writing – review and editing. Nima Rezaei: conceptualization, supervision, writing – review and editing.

Conflicts of interest

There are no conflicts to declare.

Appendices

Appendix A

The hard-chain contribution to the Helmholtz energy is described by eqn (A1):[47]

$$\tilde{a}^{\text{hc}} = \bar{m}\tilde{a}^{\text{hs}} - \sum_i x_i(m_i - 1)\ln g_{ii}^{\text{hs}} \tag{A1}$$

$\tilde{a}^{\text{hs}}$ is the dimensionless residual Helmholtz energy of the hard-sphere obtained for each segment from eqn (A2); and g_{ii}^{hs} is the radial distribution function of the hard-sphere fluid defined by eqn (A3).

$$\tilde{a}^{\text{hs}} = \frac{1}{\xi_0}\left(\frac{3\xi_1\xi_2}{(1-\xi_3)} + \frac{{\xi_2}^3}{\xi_3(1-\xi_3)^2} + \left(\frac{{\xi_2}^3}{{\xi_3}^2} - \xi_0\right)\ln(1-\xi_3)\right) \tag{A2}$$

$$g_{ij}^{\text{hs}} = \frac{1}{(1-\xi_3)} + \left(\frac{d_i d_j}{d_i + d_j}\right)\frac{3\xi_2}{(1-\xi_3)^2} + \left(\frac{d_i d_j}{d_i + d_j}\right)^2 \frac{2{\xi_2}^2}{(1-\xi_3)^3} \tag{A3}$$

The association contribution to the dimensionless residual Helmholtz energy is described by eqn (A4)–(A8):[48,54]

$$\tilde{a}^{\text{assoc}} = \sum_i x_i\left(\sum_{\mathcal{A}_i}\left(\ln X^{\mathcal{A}_i} - \frac{X^{\mathcal{A}_i}}{2}\right) + \frac{M_i}{2}\right) \tag{A4}$$

$$X^{\mathcal{A}_i} = \left(1 + \hat{\rho}\sum_j \sum_{\mathcal{B}_j} x_j X^{\mathcal{B}_j}\Delta^{\mathcal{A}_i\mathcal{B}_j}\right)^{-1} \tag{A5}$$

$$\Delta^{\mathcal{A}_i\mathcal{B}_j} = \left(\frac{\sigma_i + \sigma_j}{2}\right)^3 g_{ij}^{\text{hs}} k^{\mathcal{A}_i\mathcal{B}_j}\left(\mathrm{e}^{\frac{\varepsilon^{\mathcal{A}_i\mathcal{B}_j}}{kT}} - 1\right) \tag{A6}$$

$$\varepsilon^{\mathcal{A}_i\mathcal{B}_j} = \frac{\varepsilon^{\mathcal{A}_i\mathcal{B}_i} + \varepsilon^{\mathcal{A}_j\mathcal{B}_j}}{2} \tag{A7}$$

$$k^{\mathcal{A}_i\mathcal{B}_j} = \sqrt{k^{\mathcal{A}_i\mathcal{B}_i}k^{\mathcal{A}_j\mathcal{B}_j}}\left(\frac{2\sqrt{\sigma_i\sigma_j}}{\sigma_i + \sigma_j}\right)^3 \tag{A8}$$

where $X^{\mathcal{A}}$ is the mole fraction of molecules that are not bonded at site $\mathcal{A}$ and M_i is the number of association sites on each molecule. In this study, we consider $M_i = 2$ for all associating molecules because of using the 2B association scheme. Furthermore, $k^{\mathcal{AB}}$ and $\varepsilon^{\mathcal{AB}}$ are the associating component parameters of the PC-SAFT EoS related to the effective association volume and the association energy, respectively. For non-associating molecules, these parameters are set to zero.

Acknowledgements

The authors wish to acknowledge Jane and Aatos Erkko Foundation (JAES) in Finland for providing research funding for our project (210053) that enabled this research.

References

1 A. A. Azmi and M. A. A. Aziz, Mesoporous adsorbent for CO_2 capture application under mild condition: a review, *J. Environ. Chem. Eng.*, 2019, **7**, 103022.

2 J. Jiao, J. Cao, Y. Xia and L. Zhao, Improvement of adsorbent materials for CO_2 capture by amine functionalized mesoporous silica with worm-hole framework structure, *Chem. Eng. J.*, 2016, **306**, 9–16.

3 H. F. Hasan, F. T. Al-Sudani, T. M. Albayati, I. K. Salih, H. N. Harharah, H. S. Majdi, N. M. C. Saady, S. Zendehboudi and A. Amari, Synthesizing and Characterizing a Mesoporous Silica Adsorbent for Post-Combustion CO_2 Capture in a Fixed-Bed System, *Catalysts*, 2023, **13**, 1267.

4 F. Farjadian, A. Roointan, S. Mohammadi-Samani and M. Hosseini, Mesoporous silica nanoparticles: Synthesis, pharmaceutical applications, biodistribution, and biosafety assessment, *Chem. Eng. J.*, 2019, **359**, 684–705.

5 D. Bhatane, S. R. Pamshong, S. Sarnaik and P. A. Amit Alexander, Potential applications of mesoporous silica nanoparticles for the treatment of neurological disorders, *J. Drug Delivery Sci. Technol.*, 2023, 104970.

6 N. Kumar, A. Pandey, Rosy and Y. C. Sharma, A review on sustainable mesoporous activated carbon as adsorbent for efficient removal of hazardous dyes from industrial wastewater, *J. Water Process Eng.*, 2023, **54**, 104054.

7 H. Zhang, Y. Zhang, Y. Pan, F. Wang, Y. Sun, S. Wang, Z. Wang, A. Wu and Y. Zhang, Efficient removal of heavy

metal ions from wastewater and fixation of heavy metals in soil by manganese dioxide nanosorbents with tailored hollow mesoporous structure, *Chem. Eng. J.*, 2023, **459**, 141583.

8 D. Gang, Z. Uddin Ahmad, Q. Lian, L. Yao and M. E. Zappi, A review of adsorptive remediation of environmental pollutants from aqueous phase by ordered mesoporous carbon, *Chem. Eng. J.*, 2021, **403**, 126286.

9 Z. Taherian, A. Khataee, N. Han and Y. Orooji, Hydrogen production through methane reforming processes using promoted-Ni/mesoporous silica: a review, *J. Ind. Eng. Chem.*, 2022, **107**, 20–30.

10 P. García-Muñoz, N. P. Zussblatt, B. F. Chmelka, V. A. de la Peña O'Shea and F. Fresno, Production of hydrogen from gas-phase ethanol dehydrogenation over iron-grafted mesoporous Pt/TiO$_2$ photocatalysts, *Chem. Eng. J.*, 2022, **450**, 138450.

11 L. Ge, Y. Feng, Y. Dai, R. Wang and T. Ge, Imidazolium-based ionic liquid confined into ordered mesoporous MCM-41 for efficient dehumidification, *Chem. Eng. J.*, 2023, **452**, 139116.

12 M. Zhang, B. Sun, K. Wei Shah and X. Zhang, Molecular dynamics study on electric field-facilitated separation of H$_2$O/O$_2$ through nanoporous graphene oxide membrane, *J. Mol. Liq.*, 2022, **351**, 118634.

13 G. D. Park, J. Lee, Y. Piao and Y. C. Kang, Mesoporous graphitic carbon-TiO$_2$ composite microspheres produced by a pilot-scale spray-drying process as an efficient sulfur host material for Li–S batteries, *Chem. Eng. J.*, 2018, **335**, 600–611.

14 K. K. Gill, R. Gibson, K. H. C. Yiu, P. Hester and N. M. Reis, Microcapillary film reactor outperforms single-bore mesocapillary reactors in continuous flow chemical reactions, *Chem. Eng. J.*, 2021, **408**, 127860.

15 M. N. Gebresillase, D. Ho Hong, J.-H. Lee, E.-B. Cho and J. Gil Seo, Direct solvent-free selective hydrogenation of levulinic acid to valeric acid over multi-metal $[\mathrm{Ni}_x\mathrm{Co}_y\mathrm{Mn}_z\mathrm{Al}_w]$-doped mesoporous silica catalysts, *Chem. Eng. J.*, 2023, **472**, 144591.

16 G. Luo, Z. Li, Q. Liu, S. Guo, X. Pei, J. Lv, S. Huang, Y. Wang and X. Ma, Enhanced synthesis of C^{2+} alcohols from syngas over a Co–CO$_2$C catalyst supported on mesoporous carbon–silica composites, *Chem. Eng. J.*, 2023, **475**, 146206.

17 K. Cychosz Struckhoff, M. Thommes and L. Sarkisov, On the Universality of Capillary Condensation and Adsorption Hysteresis Phenomena in Ordered and Crystalline Mesoporous Materials, *Adv. Mater. Interfaces*, 2020, **7**, DOI: **10.1002/admi.202000184**.

18 L. R. Fisher, R. A. Gamble and J. Middlehurst, The Kelvin equation and the capillary condensation of water, *Nature*, 1981, **290**, 575–576.

19 J. Huang, X. Yin, M. Barrufet and J. Killough, Lattice Boltzmann simulation of phase equilibrium of methane in nanopores under effects of adsorption, *Chem. Eng. J.*, 2021, **419**, 129625.

20 L. R. Fisher and J. N. Israelachvili, Direct experimental verification of the Kelvin equation for capillary condensation, *Nature*, 1979, **277**, 548–549.

21 L. R. Fisher and J. N. Israelachvili, Experimental studies on the applicability of the Kelvin equation to highly curved concave menisci, *J. Colloid Interface Sci.*, 1981, **80**, 528–541.

22 I. Al-Kindi and T. Babadagli, Revisiting Kelvin equation and Peng–Robinson equation of state for accurate modeling of hydrocarbon phase behavior in nano capillaries, *Sci. Rep.*, 2021, **11**, 6573.

23 R. C. Tolman, The Effect of Droplet Size on Surface Tension, *J. Chem. Phys.*, 1949, **17**, 333–337.

24 Z. Li, Z. Jin and A. Firoozabadi, Phase Behavior and Adsorption of Pure Substances and Mixtures and Characterization in Nanopore Structures by Density Functional Theory, *SPE J.*, 2014, **19**, 1096–1109.

25 D. R. Sandoval, W. Yan, M. L. Michelsen and E. H. Stenby, Influence of Adsorption and Capillary Pressure on Phase Equilibria inside Shale Reservoirs, *Energy Fuels*, 2018, **32**, 2819–2833.

26 G. J. Zarragoicoechea and V. A. Kuz, van der Waals equation of state for a fluid in a nanopore, *Phys. Rev. E*, 2002, **65**, 021110.

27 W. Xiong, Y.-L. Zhao, J.-H. Qin, S.-L. Huang and L.-H. Zhang, Phase equilibrium modeling for confined fluids in nanopores using an association equation of state, *J. Supercrit. Fluids*, 2021, **169**, 105118.

28 L. Travalloni, M. Castier, F. W. Tavares and S. I. Sandler, Thermodynamic modeling of confined fluids using an extension of the generalized van der Waals theory, *Chem. Eng. Sci.*, 2010, **65**, 3088–3099.

29 S. Salahshoor, M. Fahes and C. Teodoriu, A review on the effect of confinement on phase behavior in tight formations, *J. Nat. Gas Sci. Eng.*, 2018, **51**, 89–103.

30 J. Wu, Density functional theory for chemical engineering: From capillarity to soft materials, *AIChE J.*, 2006, **52**, 1169–1193.

31 E. A. Ustinov and D. D. Do, Modeling of Adsorption in Finite Cylindrical Pores by Means of Density Functional Theory, *Adsorption*, 2005, **11**, 455–477.

32 T. Ren, C.-Y. Wang, R. Huang, C. Deng, Y. Xu, A. Majumder, J. Ra, K. Shen, J. M. Vohs, J. J. de Pablo, R. J. Gorte and D. Lee, Understanding polymer-porous solid interactions based on small gas molecule adsorption behavior, *Chem. Eng. J.*, 2023, **473**, 145220.

33 Y. Liu, Z. Jin and H. A. Li, Comparison of Peng–Robinson Equation of State With Capillary Pressure Model With Engineering Density-Functional Theory in Describing the Phase Behavior of Confined Hydrocarbons, *SPE J.*, 2018, **23**, 1784–1797.

34 M. Sedghi and M. Piri, Capillary condensation and capillary pressure of methane in carbon nanopores: Molecular Dynamics simulations of nanoconfinement effects, *Fluid Phase Equilib.*, 2018, **459**, 196–207.

35 H. Hu, Q. Li, S. Liu and T. Fang, Molecular dynamics study on water vapor condensation and infiltration characteristics in nanopores with tunable wettability, *Appl. Surf. Sci.*, 2019, **494**, 249–258.

36 M. B. Asadi, A. De Rosis and S. Zendehboudi, Central-Moments-Based Lattice Boltzmann for Associating Fluids:

A New Integrated Approach, *J. Phys. Chem. B*, 2020, **124**, 2900–2913.

37 Y. Wang and S. A. Aryana, Coupled confined phase behavior and transport of methane in slit nanopores, *Chem. Eng. J.*, 2021, **404**, 126502.

38 G. J. Zarragoicoechea and V. A. Kuz, Critical shift of a confined fluid in a nanopore, *Fluid Phase Equilib.*, 2004, **220**, 7–9.

39 S. P. Tan and M. Piri, Equation-of-state modeling of confined-fluid phase equilibria in nanopores, *Fluid Phase Equilib.*, 2015, **393**, 48–63.

40 M. Thommes and G. H. Findenegg, Pore Condensation and Critical-Point Shift of a Fluid in Controlled-Pore Glass, *Langmuir*, 1994, **10**, 4270–4277.

41 K. Morishige and M. Shikimi, Adsorption hysteresis and pore critical temperature in a single cylindrical pore, *J. Chem. Phys.*, 1998, **108**, 7821–7824.

42 L. Travalloni, M. Castier, F. W. Tavares and S. I. Sandler, Critical behavior of pure confined fluids from an extension of the van der Waals equation of state, *J. Supercrit. Fluids*, 2010, **55**, 455–461.

43 M. B. Asadi and S. Zendehboudi, Hybridized method of pseudopotential lattice Boltzmann and cubic-plus-association equation of state assesses thermodynamic characteristics of associating fluids, *Phys. Rev. E*, 2019, **100**, 043302.

44 J. O. Valderrama and P. A. Robles, Critical Properties, Normal Boiling Temperatures, and Acentric Factors of Fifty Ionic Liquids, *Ind. Eng. Chem. Res.*, 2007, **46**, 1338–1344.

45 J. Prausnitz, R. Lichtenthaler and E. G. de Azevedo, *Molecular Thermodynamics of Fluid-Phase Equilibria*, Prentice Hall PTR, New Jersey, 3ed edn, 1999.

46 S. P. Tan and M. Piri, Retrograde behavior revisited: implications for confined fluid phase equilibria in nanopores, *Phys. Chem. Chem. Phys.*, 2017, **19**, 18890–18901.

47 J. Gross and G. Sadowski, Perturbed-Chain SAFT: An Equation of State Based on a Perturbation Theory for Chain Molecules, *Ind. Eng. Chem. Res.*, 2001, **40**, 1244–1260.

48 J. Gross and G. Sadowski, Application of the Perturbed-Chain SAFT Equation of State to Associating Systems, *Ind. Eng. Chem. Res.*, 2002, **41**, 5510–5515.

49 A. A. Shapiro and E. H. Stenby, Kelvin equation for a non-ideal multicomponent mixture, *Fluid Phase Equilib.*, 1997, **134**, 87–101.

50 R. J. Stokes and D. F. Evans, *Fundamentals of Interfacial Engineering*, Wiley, Germany, 1997.

51 G. Yang, Z. Fan and X. Li, Determination of confined fluid phase behavior using extended Peng–Robinson equation of state, *Chem. Eng. J.*, 2019, **378**, 122032.

52 G. Yang, Z. Fan and X. Li, Determination of confined fluid phase behavior using extended Peng–Robinson equation of state, *Chem. Eng. J.*, 2019, **378**, 122032.

53 J. Gross and G. Sadowski, Reply to Comment on ''Perturbed-Chain SAFT: An Equation of State Based on a Perturbation Theory for Chain Molecules'', *Ind. Eng. Chem. Res.*, 2019, **58**, 5744–5745.

54 W. G. Chapman, K. E. Gubbins, G. Jackson and M. Radosz, New reference equation of state for associating liquids, *Ind. Eng. Chem. Res.*, 1990, **29**, 1709–1721.

55 W. A. Cañas-Marín, D. L. González and B. A. Hoyos, Comment on ''Perturbed-Chain SAFT: An Equation of State Based on a Perturbation Theory for Chain Molecules'', *Ind. Eng. Chem. Res.*, 2019, **58**, 5743.

56 L. Kong and H. Adidharma, Adsorption of simple square-well fluids in slit nanopores: Modeling based on Generalized van der Waals partition function and Monte Carlo simulation, *Chem. Eng. Sci.*, 2018, **177**, 323–332.

57 L. Travalloni, M. Castier, F. W. Tavares and S. I. Sandler, Thermodynamic modeling of confined fluids using an extension of the generalized van der Waals theory, *Chem. Eng. Sci.*, 2010, **65**, 3088–3099.

58 K. Morishige, N. Tateishi and S. Fukuma, Capillary Condensation of Nitrogen in MCM-48 and SBA-16, *J. Phys. Chem. B*, 2003, **107**, 5177–5181.

59 K. Morishige and M. Ito, Capillary condensation of nitrogen in MCM-41 and SBA-15, *J. Chem. Phys.*, 2002, **117**, 8036–8041.

60 K. Morishige, H. Fujii, M. Uga and D. Kinukawa, Capillary Critical Point of Argon, Nitrogen, Oxygen, Ethylene, and Carbon Dioxide in MCM-41, *Langmuir*, 1997, **13**, 3494–3498.

61 K. Morishige and Y. Nakamura, Nature of Adsorption and Desorption Branches in Cylindrical Pores, *Langmuir*, 2004, **20**, 4503–4506.

62 M. Thommes, R. Köhn and M. Fröba, Sorption and Pore Condensation Behavior of Nitrogen, Argon, and Krypton in Mesoporous MCM-48 Silica Materials, *J. Phys. Chem. B*, 2000, **104**, 7932–7943.

63 E. Barsotti, S. Saraji, S. P. Tan and M. Piri, Capillary Condensation of Binary and Ternary Mixtures of *n*-Pentane–Isopentane–CO_2 in Nanopores: An Experimental Study on the Effects of Composition and Equilibrium, *Langmuir*, 2018, **34**, 1967–1980.

64 X. Qiu, S. P. Tan, M. Dejam and H. Adidharma, Isochoric measurement of the evaporation point of pure fluids in bulk and nanoporous media using differential scanning calorimetry, *Phys. Chem. Chem. Phys.*, 2020, **22**, 7048–7057.

65 E. Barsotti, S. P. Tan, M. Piri and J.-H. Chen, Phenomenological Study of Confined Criticality: Insights from the Capillary Condensation of Propane, *n*-Butane, and *n*-Pentane in Nanopores, *Langmuir*, 2018, **34**, 4473–4483.

66 S. Z. Qiao, S. K. Bhatia and D. Nicholson, Study of Hexane Adsorption in Nanoporous MCM-41 Silica, *Langmuir*, 2004, **20**, 389–395.

67 N. Tanchoux, P. Trens, D. Maldonado, F. Di Renzo and F. Fajula, The adsorption of hexane over MCM-41 type materials, *Colloids Surf., A*, 2004, **246**, 1–8.

68 E. Van Bavel, V. Meynen, P. Cool, K. Lebeau and E. F. Vansant, Adsorption of Hydrocarbons on Mesoporous SBA-15 and PHTS Materials, *Langmuir*, 2005, **21**, 2447–2453.

69 H. Vinh-Thang, Q. Huang, M. Eić, D. Trong-On and S. Kaliaguine, Adsorption of C_7 Hydrocarbons on Biporous SBA-15 Mesoporous Silica, *Langmuir*, 2005, **21**, 5094–5101.

70 C. Nguyen, C. G. Sonwane, S. K. Bhatia and D. D. Do, Adsorption of Benzene and Ethanol on MCM-41 Material, *Langmuir*, 1998, **14**, 4950–4952.

71 M. M. L. Ribeiro Carrott, A. J. E. Candeias, P. J. M. Carrott, P. I. Ravikovitch, A. V. Neimark and A. D. Sequeira, Adsorption of nitrogen, neopentane, *n*-hexane, benzene and methanol for the evaluation of pore sizes in silica grades of MCM-41, *Microporous Mesoporous Mater.*, 2001, **47**, 323–337.

72 S. Kittaka, S. Ishimaru, M. Kuranishi, T. Matsuda and T. Yamaguchi, Enthalpy and interfacial free energy changes of water capillary condensed in mesoporous silica, MCM-41 and SBA-15, *Phys. Chem. Chem. Phys.*, 2006, **8**, 3223.

73 J. S. Oh, W. G. Shim, J. W. Lee, J. H. Kim, H. Moon and G. Seo, Adsorption Equilibrium of Water Vapor on Mesoporous Materials, *J. Chem. Eng. Data*, 2003, **48**, 1458–1462.

74 K. Morishige, T. Kawai and S. Kittaka, Capillary Condensation of Water in Mesoporous Carbon, *J. Phys. Chem. C*, 2014, **118**, 4664–4669.

75 X. Qiu, H. Yang, M. Dejam, S. P. Tan and H. Adidharma, Experiments on the Capillary Condensation/Evaporation Hysteresis of Pure Fluids and Binary Mixtures in Cylindrical Nanopores, *J. Phys. Chem. C*, 2021, **125**, 5802–5815.

76 J.-H. Yun, T. Düren, F. J. Keil and N. A. Seaton, Adsorption of Methane, Ethane, and Their Binary Mixtures on MCM-41: Experimental Evaluation of Methods for the Prediction of Adsorption Equilibrium, *Langmuir*, 2002, **18**, 2693–2701.

77 Y. He and N. A. Seaton, Experimental and Computer Simulation Studies of the Adsorption of Ethane, Carbon Dioxide, and Their Binary Mixtures in MCM-41, *Langmuir*, 2003, **19**, 10132–10138.

78 Q. Yang, P. Z. Sun, L. Fumagalli, Y. V. Stebunov, S. J. Haigh, Z. W. Zhou, I. V. Grigorieva, F. C. Wang and A. K. Geim, Capillary condensation under atomic-scale confinement, *Nature*, 2020, **588**, 250–253.

79 S. Gast, J. H. Matthies, U. S. Tuttlies and U. Nieken, A Novel Experimental Setup for Kinetic Studies of Toluene Oxidation in the Homogeneous Liquid Phase, *Chem. Eng. Technol.*, 2017, **40**, 1445–1452.

80 O. R. Quayle, The Parachors of Organic Compounds. An Interpretation and Catalogue, *Chem. Rev.*, 1953, **53**, 439–589.

81 M. Ma, S. Chen and J. Abedi, Binary interaction coefficients of asymmetric CH_4, C_2H_6, and CO_2 with high *n*-alkanes for the simplified PC-SAFT correlation and prediction, *Fluid Phase Equilib.*, 2015, **405**, 114–123.

82 J. Wu, H. Zhou, H. Wang, H. Shao, G. Yan and T. Lin, Novel Water Harvesting Fibrous Membranes with Directional Water Transport Capability, *Adv. Mater. Interfaces*, 2019, **6**, DOI: **10.1002/admi.201801529**.